

Microbial vs thermogenic gas hydrates in the South Falkland Basin: BSR distribution and fluid origin

M. Foschi^{1*}, M. Paganoni², J.A. Cartwright¹ and E. Idiz¹

¹ Department of Earth science, University of Oxford, South Parks Road, Oxford, OX1 3AN, UK

² Shell Projects & Technology, 40 Lange Kleiweg, Rijswijk, 2288 GK, The Netherlands

*martinof@earth.ox.ac.uk

Abstract

The South Falkland Basin hosts a working petroleum system, as well as one of the most recently discovered gas hydrate provinces of the South Atlantic Ocean. Using three-dimensional reflection seismic data, a series of bottom-simulating reflections (BSRs) are interpreted within two contrasting settings, (1) the thrust-cored anticlines, developed by the oblique convergence of the Scotia and the South American plates, and (2) the foreland basin, formed to the north of this plate boundary. These BSRs are interpreted as the base of the gas hydrate stability zone, and are associated with seismic indicators of underlying free-gas accumulations and overlying hydrate-bearing sediments.

In the foreland basin, the BSR is laterally continuous for tens of kilometres, whereas in the fold belt, BSR occurrences are restricted to limited portions of the thrust-cored anticline crests. These observations, calibrated with sedimentological analyses and gas geochemistry, argue that the gas source for the gas hydrates within the thrust-cored anticlines is unrelated to in-situ microbial generation of methane, but instead is associated with the vertical seepage of thermogenic fluids from deeper cores of the anticlines. In contrast, the nature of the sediments in the foreland basin appears more favourable for the generation of shallow microbial methane.

This study highlights that, in specific tectonic and depositional environments, the character of the BSR observed on reflection seismic data with the limited support of in-situ data, can be used to predict the most likely source of natural gas hydrate systems.

Keywords

Gas Hydrate; Bottom Simulating Reflection; Hydrocarbon Plumbing System; Microbial Gas; Thermogenic Gas; Hydrocarbon Migration;

1 Introduction

The occurrence of natural gas hydrates (GH) is controlled by thermobaric and geochemical conditions and is confined to certain portions of continental margins and permafrost regions, whereby water combines with light gas phases, typically methane, in excess of saturation (Xu and Ruppel, 1999; Collett et al., 2009). The occurrence of GH is commonly inferred on seismic data by the identification of bottom-simulating reflections (BSRs), which approximate the base of the gas hydrate stability zone (BGHSZ) (Holbrook et al., 1996). BSRs reflect a negative acoustic impedance contrast between hydrate and free gas-bearing sediments, the latter constituting the so-called free gas zone (FGZ) (Bangs et al., 1993; Plaza-Faverola et al., 2012; Hillman et al., 2017).

Because the occurrence of GH is primarily linked to the availability of light hydrocarbons in excess of their saturation in pore waters (Xu and Ruppel, 1999), it is paramount to understand the plumbing system of these gas phases and integrate it with the sedimentary and structural history of the basin. The origin of the gas responsible for the formation of hydrates is usually the result of variable mixtures of microbial methane and other light hydrocarbons generated in the first ~1-2 km of overburden, with thermogenic methane-dominated gases, generated by the cracking of organic matter deeper in the sedimentary column (Milkov, 2005).

Critical factors controlling the availability of microbial methane are represented by the amount of metabolizable organic carbon, as well as by its reaction rate and burial preservation (Davie and Buffett, 2001; Wallmann et al., 2006; Pohlman et al., 2009; Malinverno, 2010). In contrast thermogenic hydrocarbons are controlled by the long-term history of the basin (burial and temperature), which controls their generation from potential source rocks and the presence of adequate migration pathways for methane-rich fluids towards the gas hydrate stability zone (GHSZ). At the km-scale, these microbial and thermogenic components become active parts of hydrocarbon plumbing systems, characterised by multi-phase flows along stratal and cross-stratal permeable routes (Magoon and Dow, 1994; Cartwright et al., 2007; Collett et al., 2009; Løseth et al., 2009; Andresen, 2012).

The integration of geochemical data and seismic observations holds the key to understanding the nature of the hydrate sourcing fluids, as previously demonstrated in studies from different geological settings worldwide (e.g. Borowski, 2004; Milkov et al., 2005; Riedel et al., 2010b; Ruffine et al., 2013; Smith et al., 2014; Paganoni et al., 2016). Furthermore, recent studies of microbial and thermogenic gas production and migration into the GHSZ in diverse geological settings indicate that both microbial and thermogenic methane contribute to hydrate formation (Kroeger et al., 2015; Dumke et al., 2016; Burwicz et al., 2017). To date, there have been few studies on natural gas hydrate systems in basins away from major continental margins and therefore far from sources of organic matter and high volumes of sediment input, i.e. key elements for recent microbial generation of methane (Nole et al., 2017).

In this study, the occurrence of GHs in the South Falkland Basin (SFB), recently identified as a new gas hydrate province in the South Atlantic Ocean (Foschi and Cartwright, 2016), is documented with the aim to understand the relationship between the depositional environment, the hydrocarbon migration system and GH distribution. The fold and thrust belt developed along this margin is far from major sources of terrigenous sediments and is subjected to the erosive action of the Antarctic Circumpolar Current (Bry et al., 2004; Pérez et al., 2015). The lateral extent of the BSRs, in the studied portion of the margin, is shown to be unusually restricted. Our geophysical and lithological observations, calibrated with gas geochemistry, raises the possibility that, in certain scenarios, the distribution of BSRs can be used to predict the likely source of the gas phases forming the GHs.

2 Data, methods and geological setting

2.1 Data and methods

The 3D seismic survey used in this study is located in the SFB and covers an area of 1650 km² (Fig. 1). The seismic data, provided by Borders and Southern Petroleum PLC, were processed to zero phase and American polarity, where an increase of acoustic impedance with depth is represented by a positive reflection (white-black-white; w-b-w, Fig. 1C inset). The dominant seismic frequency is 40 Hz, yielding a vertical resolution of 10 m (Widess, 1973). Trace spacing is 25 m. The 3D volume was depth converted

using a root-mean square velocity field provided by Borders and Southern Petroleum PLC. This operation was completed using Landmark's ProMAX 3D. The BSR was interpreted using standard criteria: (1) crudely mimics the seafloor bathymetry, (2) polarity opposite to that of the seabed (black-white-black; b-w-b, Fig.1C inset) and (3) variably discordant to host stratal reflections (e.g. Baba and Yamada, 2004; Hillman et al., 2017; Shedd et al., 2012). This operation was completed using Schlumberger's Petrel software.

A set of surfaces representing the base of the gas hydrate stability zones (mBGHSZ) were modelled using CSMHYD software (Sloan and Koh, 2008). The mBGHSZs were calculated using temperature and salinity profiles collected in the water column in the study area (ranges: 2.2 – 4.7°C and 34.1 – 34.75 psu; see Supplementary Figure 1) (provided by Borders and Southern Petroleum PLC). Flattening of the 3D depth converted seismic survey was carried out to highlight potential discordant trends between the BSR and the seabed. This operation was completed using the seabed as datum.

Physical properties and geochemical information of the shallow sub-seafloor sediments were completed by Benthic Solution Limited, at 23 benthic stations (Fig. 1), by means of 0.25 m² USNEL type box corers, 0.20 m² Van Veen Grab samplers and 3 m gravity corers. The data, made available by Borders and Southern Petroleum PLC, include particle size distribution, such as median, fraction percentages, sorting and skewness. The data included also the measurement of the total organic carbon (TOC) in the sediments.

Headspace gas data were collected from the borehole 61/25-1 and made available by Borders and Southern Petroleum PLC. The data was collected using Isotech's IsoTube and IsoJar techniques (www.isotechlabs.com). The IsoTube method collects gas samples directly at the wellhead, while IsoJar allows storing gas present in washed cuttings, after collection from the shale shaker. The gas obtained from these two techniques were used to calculate gas wetness (c.f. Haworth et al., 1985) and $\delta^{13}\text{C}$ from methane. TOC values along the boreholes 61/25-01 were also available and used to constrain the variation of organic carbon with depth.

2.2 Geological setting

The study area is located about 200 km to the south of the Falkland Islands (FI, Fig. 1A), between the Burdwood Bank to the south and the foreland portion of the SFB to the north (Fig. 1B) (Platt and Philip, 1995; Bry et al., 2004; Foschi and Cartwright, 2016). The belt comprises a series of thrust-propagation anticlines, whose axes strike approximately ESE-WNW (Fig. 1B). These structures are the consequence of sinistral transpressive shortening and caused the loading of the South American Plate on the Scotia Plate, along the Scotia-South America plate boundary (SSAPB, Fig. 1A) (Bry et al., 2004). The formation of the fold and thrust belt and the related foredeep is diachronous along the entire transpressive margin and, in the study area, is thought to have commenced in the early Paleogene (~50 Ma), up to present day (Bry et al., 2004).

The interval of interest (II), from the seabed to about 1500 m below it (Fig. 1C), comprises clay-rich pelagic and hemipelagic Cenozoic successions. These successions, encountered along the borehole 61/25-1 (from 2115 m TVDSS), exhibit parallel to sub-parallel reflections on seismic sections, as well as undulating patterns typical of contourite drift deposits (Fig. 1C; Koenitz et al., 2008; Rebesco et al., 2014). These drifts are eroded and/or not deposited along the crests of the anticlines, due to the joint action of circumpolar currents, tectonic uplift, and deactivation of the axial Andean sediment supply. The deformation of these structures, in conjunction with the lack of sediment drapes along the anticlinal ridges, allowed the exposure of sediments at least 5 Ma old at the seabed (c.f. Ghiglione et al., 2010).

A number of laterally and vertically extensive mass transport deposits (MTDs, Fig. 1C), with variable thickness of ~100-300 m, are observed on seismic data within the II. These exhibit chaotic facies and irregular top and bottom surfaces (cf. Posamentier and Martinsen, 2011). These are mainly developed and stacked in the foredeep to the north of the anticlines, where they dominate, together with hemipelagic and pelagic laterally continuous sequences, the Cenozoic sedimentary infill. Recent reconstructions (Ghiglione et al., 2010) date the II as Eocene to Miocene in age, although Plio-Pleistocene drift sediments, turbidites and hemipelagites are present in the mini-basins located between the anticlines (MB; Fig. 1C), as well as

in the foreland basin, located northwestwardly with respect to the fold and thrust belt (Bry et al., 2004; Koenitz et al., 2008; Foschi and Cartwright, 2016).

The SFB hosts a working petroleum system (Fish, 2005). Hydrocarbon accumulations discovered to date comprise the Darwin gas condensate fields (East and West) with an estimated un-risked recoverable resource of 432 million barrels of oil equivalent (Borders and Southern, 2018). The hydrocarbons encountered in the Darwin fields are interpreted to have been generated by Jurassic and Lower Cretaceous source rocks.

3 Results

3.1 Geophysical observations

The 3D seismic interpretation revealed the occurrence of BSRs in several regions within the II (Figs. 1B, 2A-E, 3A). All the BSR regions, with the exception of BSR-1, are located along the southernmost portion of the study area and strike approximately E-W. BSR-1 is located to the NW corner of the study area (Fig. 1B), within the recent sedimentary infill of the foreland basin, and represents only a portion of a larger BSR (Fig. 1D) with a total approximate extent of 3350 km² (based on 2D seismic data; Foschi and Cartwright, 2016).

On seismic cross section BSRs 2 to 6 are hosted mostly within fine-grained intervals, such as those penetrated by well 61/25-1. BSR-1 is instead almost entirely hosted by the more recently deposited MTDs within the foreland region of the study area (Fig. 1B). All the BSRs (1) exhibit opposite polarity with respect to the seabed, (2) cross cut the back ground stratigraphy, but (3) do not always mimic the bathymetry (Fig. 2). This characteristic is observed on those BSRs with modest lateral extent, such as BSRs 5 and 6 (Fig. 2A). These BSRs are relatively flat as observed on seismic section and show a discordant trend with the bathymetry (Fig. 2B). BSR-1 and BSR-3 are instead better developed and mimic precisely the seabed morphology (Fig. 2C, 2D and 2E).

The lateral extent of the encountered BSRs is occasionally associated with depositional complexities, such as for BSR-3, which is limited to the north by the top surface of an MTD (Fig. 2E). However, no evident depositional features seem to limit the extent of BSR-2 to 6. This can be clearly seen by observing any of the laterally continuous reflections hosting BSR 5 and 6 (Fig. 2A). Interestingly, BSR-1 cross-cuts two MTDs in the foreland basin at the front of the fold and thrust belt. In this case BSR-1 maintains its continuity along the MTD and is not shifted or interrupted by lithology and facies changes (Fig. 2C and 2D).

Anomalous amplifications of the background stratigraphy are observed beneath BSRs 1, 3 and 4 (e.g. Fig. 2A, 2D 2E). These are systematically limited at the top by the BSRs and by amplitude cut-offs at the base. The amplitude cut off fades out gradually below BSR-1 (Fig. 2C) while sharp amplitude cut offs characterised by a positive polarity are observed below BSR-3 (Fig. 2E). These positive reflections (1) cross cut the background stratigraphy (as the BSR), (2) do not simulate the shape of the seabed, and (3) are rather flat reflections, such as flat spots associated to gas water contacts. These amplified regions resemble previously identified zones with free gas typically associated with methane trapped underneath the gas hydrate bearing sediments (free gas zone, FGZ; cf. Grauls, 2001; Boswell et al., 2012; Taladay et al., 2017). FGZ-3 is the most extensive FGZ in the study area with a maximum thickness of about 160 m (Fig. 2E).

Based on the above geophysical evidence, namely polarity, cross cutting relationship with host reflectivity, seabed-simulating character, and FGZs (e.g. Baba and Yamada, 2004; Shedd et al., 2012; Hillman et al., 2017), the documented BSRs are interpreted as the base of the gas hydrate accumulations.

3.2 Modelling of the base of the gas hydrate stability zone

Modelling of the BGHSZ (mBGHSZ) was carried out in order to establish whether the observed BSRs are actually the base of gas hydrate occurrences, and, importantly, if these are consistent with the in-situ temperature-pressure conditions and gas composition.

BSR-1 and 1a are located along the mBGHSZs for gas hydrates composed of 100% methane at a geothermal gradient between 35 and $40^{\circ}\text{C} \cdot \text{km}^{-1}$ (Fig. 2C, 2D). BSR-1 and 1a are located near the exploration borehole 61/17-01 where a geothermal gradient of $35.47^{\circ}\text{C} \cdot \text{km}^{-1}$ was observed. Because heavier hydrocarbons would shift the BGHSZ downward (Milkov and Sassen, 2001), BSR-1 and 1a are interpreted to be necessarily formed by a gas mixture dominated by methane.

BSRs 2 to 6 are instead located along the mBGHSZs for gas hydrates stable at much higher geothermal gradients (gas mixture of 100% methane). BSR-3 fall along the mBGHSZ obtained with a geothermal gradient of $45^{\circ}\text{C} \cdot \text{km}^{-1}$ (Fig. 2E) while BSR-5 falls along the mBGHSZ consistent with a geothermal gradient of $55^{\circ}\text{C} \cdot \text{km}^{-1}$ (Fig. 2A). BSR-4 is located just 1.8 km distance to the borehole 61/25-1, where during logging operations a geothermal gradient of $29.1^{\circ}\text{C} \cdot \text{km}^{-1}$ was measured (Fig. 3A). However, BSR-4 is located along the mBGHSZ consistent with a geothermal gradient of $50^{\circ}\text{C} \cdot \text{km}^{-1}$. This implies that BSR-4 is located shallower, by about 200 m, with respect to its stability conditions at the observed geothermal gradient and with a gas composition of 100% methane.

These results point out that only the BGHSZ associated with BSR-1 is located at the expected depth. The other BSRs located along the anticlinal crests are instead shallower with respect to their calibrated (BSR-4)/modelled (BSR-5, BSR-6) depths. Local variations in gas composition and salinity (and pore-size) can produce substantial vertical shifts of the position of the stability field of GHs (Milkov and Sassen, 2001; Hillman et al., 2018). However these have moderate effects and cannot justify a shift of over 200 m. The character of BSR-4, BSR-5 and BSR-6 could be explained by the fact that along the anticlines, where these BSRs are detected, the shallow sedimentary section is eroded/non-deposited and that the relative BGHSZs are not in equilibrium (relict). This can be evinced by looking at BSRs 5, 6 and 6a on the flattened seismic cube of Figure 2B. BSR-5, which is apparently stable at a geothermal gradient of $55^{\circ}\text{C} \cdot \text{km}^{-1}$, is located below a region of strong erosion at the seabed while BSRs 6 and 6a, apparently stable at lower geothermal gradients, are located below a region covered by more recently deposited/non-eroded sediments (horizon R for reference, Fig. 2B).

Although the results reveal a 200 m vertical offset between the model results and the observations, the lack of key information, such as local geothermal gradients, age calibration, sedimentation rate and erosion does not allow further description and discussion about the depths of the documented BSRs. Nonetheless, based on their seismic character (previous section) the BSRs in this region are still interpreted as BGHSZs.

3.3 Lithology and Total Organic Carbon content of seafloor sediments and borehole 61/25-1

Particle size analysis indicate a marked difference between the sediments deposited at the seabed in the folds and thrust belts and those in the foreland basin at the front of the deformed area (Table 1a). Station 23, located in the flat basinal part of the study area, is characterised by the highest concentration of clay particles (i.e. $< 2\mu\text{m}$, 79%), the lowest concentration of silty and sandy particles (i.e. $2\mu\text{m}$ -1 mm, 21%), and by a total absence of coarse sands and gravels. Being mainly characterised by fine-grained sediments, the cored material at this station unsurprisingly displays also the highest TOC (0.6%) of the study area (Table 1b). The immediately surrounding stations, in the deepest and tectonically younger folds (i.e. 12, 13, 14, 22) are characterised by similar percentages of fine-grained (i.e. clay) and coarse-grained (i.e. silts, sands, and gravel) sediments, and TOC values ranging between 0.32% and 0.51% (Table 1b). Moving south and east, in the stations located at the crests of the shallower anticlines (e.g. 1, 3, 6, 17, Fig. 1B), the shallow sediments are predominantly characterised by 60 - 90% silt, sand and gravel particles, with only subordinate clay material. In these locations, the TOC within the recovered sediment is 0.28% on average, with maximum and minimum values of 0.4% (station 10) and 0.18% (station 5, Table 1a-b). A relatively good linear relationship between the percentage of clay particles and the TOC of the recovered cores is observed at least in the sediments near the seabed.

Along the borehole 61/25-1 higher TOC values are observed in the interval 2115 and 3035 m TVDSS (522 – 1442 m below seafloor) (Fig. 3B). The TOC values from the well have been integrated with those observed at the seabed near the well at stations 6 (offset 5.5 km; water depth of 1423-1428 m), 7 (offset

4.7 km; water depth of 1534 m.), and 18 (offset 8.7 km; water depth 1745 m). The combination of these two datasets shows that a generally linear increase of TOC with depth is present ($R^2 = 0.6$, Fig. 3B) around the well location.

3.4 Molecular and isotopic composition of mud gases

Multiple sources of data provide geochemical constraints to assess the potential nature of the fluids present in the middle-to-shallow section of the thrust-cored anticlines of the SFB. IsoTube and IsoJar headspace gas analyses were performed on gas samples collected at well 61/25-01 within a depth interval of 2220 - 2815 m TVDSS. The data collected immediately below the MTD shows that the gas wetness (W_h) expressed as $(C_1 / C_2 + C_3)$, increases towards the inner core of the anticlines with values well above 20 (oil related fluids) in the entire section below 2400 m TVDSS (Fig. 3C). Cross-plotting the gas wetness ($C_1 / C_2 + C_3$) versus methane carbon isotope ($\delta^{13}C$ (‰)) and following recent classifications for genetic gas fields (Milkov and Etiope, 2018), reveals that the origin of the gas is early thermogenic and evolves towards mature thermogenic with depth (Fig. 4A). This region of the gas fields overlap also with the secondary microbial gas field which might indicate biodegradation of petroleum initially in place in these regions (Fig. 4A-B).

This geochemical information argues that thermogenic gas was delivered towards the shallow section of the basin attesting to the presence of a working thermogenic hydrocarbon system not only in the foreland basin (c.f. Fish, 2005; Foschi and Cartwright, 2016), but also in the thrust-fold anticlines of the SFB. Importantly, primary microbial gases was not found between 2220 - 2815 m TVDSS (522 – 1442 m below seafloor), although the TOC measured in the II were probably sufficient to trigger microbial methanogenesis (discussed later).

4 Discussion and implications

4.1 Settings for the formation of gas hydrates in the South Falkland Basin

The geophysical and geochemical evidence described above indicate the presence of two different geological settings in the study area where gas hydrates occur: (1) the anticlines of the thrust-fold belt, and (2) the foreland basin.

The anticlines are characterised by negligible sedimentation rates and pronounced erosion. This is associated with a generally coarser particle size from silt to gravel (Table 1a) and lower TOCs (Table 1b) in the sediments at/near the seafloor. The low TOCs reflect a higher energy environment resulting in the lack of fine-grained, clay-rich sediments and an environment that is unfavourable for the preservation of organic matter from early degradation and oxidation (Bergamaschi et al., 1997; Hedges et al., 1997). Although TOCs observed along the borehole 61/25-01 may be sufficiently high to trigger methanogenesis, primary microbial methane was not detected in the core of the anticline. The formation of gas hydrates and shallow free gas beneath the BGHSZs in the anticlines argues that hydrocarbons are probably supplied from deeper sources, thermogenic in origin but also from biodegraded petroleum.

In contrast, the foreland basin is characterised by finer particle sizes (Table 1a). The higher amount of fine-grained sediments, the lack of erosional structures and the deposition of stacked MTDs (Fig. 2C, 2D) probably enhanced preservation of organic matter, as evidenced by the generally higher TOC observed near the seafloor at stations 23 and 13 (Table 1b). This suggests that in this region if the organic matter is not completely oxidised in the first few metres of overburden (e.g. by sulphate reduction; Borowski et al., 2004; Pohlman et al., 2009), primary microbial methane could form in-situ within the GHSZ, and result in hydrate formation (Malinverno, 2010; Malinverno and Goldberg, 2015). Unfortunately, a TOC profile is not available in this region to extend this argument to the deeper portion of the basin and to, at least, the section where GHs are observed (~470 m below seafloor, Fig. 2C). However, after the initiation of the foreland basin in the early Paleogene (~50 Ma, Bry et al., 2004), the depositional setting capturing the sedimentary packages has remained unchanged to the present day. This is highlighted by the fact that the first 1000 m of shallow infill of the foredeep is characterised by the same

consistent seismic facies. Therefore, we postulate that this entire section is likely to have better microbial methanogenesis potential compared to the anticlines of the thrust-fold belt.

The seismic character of BSRs is markedly different in these two settings, particularly in terms of continuity and relation with tectonic structure. This raises the following questions: (1) why are the BSRs restricted in the fold belt in the upper portions of the anticlines, and (2) why is the BSR in the foreland basin more continuous, even across strong structural and sedimentological heterogeneities, such as the MTDs (Fig. 2A)?

4.2 Migration processes and gas hydrate distribution

The formation and the distribution of gas hydrates is controlled by the availability of hydrocarbons, in excess of saturation (Xu and Ruppel, 1999). Because light hydrocarbons, such as methane, can migrate as both a free phase gas (advection) and in solution (diffusion and/or flow in solution), contrasting distributions of gas hydrates may result as a function of one process or the other. These are briefly discussed using methane as the primary gas hydrate forming hydrocarbon phase.

When methane is flowing in solution, it is not sensitive to the capillary entry pressure of the hosting media (water-wet) and to the eventual reductions of permeability induced by multi-phase flow and hydrate formation (Bear, 1972). This suggests that methane migrates in solution until super-saturation induces the segregation of the gas from water to form free-gas accumulations or GHs (Liu and Flemings, 2006). The migration in solution is, therefore, likely to better distribute hydrocarbons across structural and stratigraphic barriers producing hydrate occurrences characterised by substantial lateral continuity.

When methane migrates as a free-phase gas, it is instead restricted to those pathways where the capillary entry pressure is sufficiently high to allow advection (Berg, 1975). Migration across low-permeability formations may still occur and requires overpressures in order for the gas to breach eventual sealing units and form hydraulic fractures or pipes (Cartwright and Santamarina, 2016). Because the

advection of free-phase gas is restricted to carrier beds, the eventual distribution of GHs will reflect the restricted or focussed distribution of available gas phases (c.f. Hillman et al., 2017)

4.3 Gas hydrate systems in the South Falkland Basin

Based on these points, we can make the following observations about the likely migration processes taking places in the two settings (foreland basin and the thrust-fold anticlines) observed in the SFB.

BSR-1, in the foreland basin, is observed cross-cutting prominent structural heterogeneities such as the stacked MTDs (Fig. 2A). If microbial gas production took place in the foreland basin, not only would the eventual dissemination of microbial sources have favoured a widespread distribution of microbial gas clusters in this region (Fig. 5A), but it would also likely have initiated a condition of under-saturation (Clayton, 1992) of microbial gas in the pore-water, favouring a further spreading of gas while in solution (Fig. 5B). These two conditions, which are likely to occur in an initial stage of microbial gas generation and migration, will produce widespread formation of GHs (Fig. 5C).

In the thrust fold belt anticlines, geochemical results point to the lack of primary microbial gas, even though the observed relative increase in TOC with depth probably would have been sufficient to promote microbial methanogenesis. Even though primary microbial gas may have still been produced in small quantities, most of the primary microbial gas in solution would have been migrated across the gas hydrate stability zone (Haacke et al., 2007) and further dissolved into the water column (Fig. 6A).

The presence of deep thermogenic and secondary microbial hydrocarbons in deeper parts of the basin was confirmed on the core of the anticlines and suggest that these were the main source for GHs in this setting. The delivery of hydrocarbons towards the GHSZ is likely to have occurred below the thrust-fold anticlines in the coarse-grained dipping intervals (i.e. carrier-beds, Fig. 6B), where free gas and hydrates may eventually have concentrated (cf. Milkov et al., 2005; Crutchley et al., 2015). Concurrently, cross-stratal pathways within the core of the anticlines may also be present, as inferred by the presence of AAs below BSR-4 (Fig. 3A). The distribution of BSR-2 to -6, at the backlimbs and crests of the anticlines (Figs. 1B and 2A) suggests that the gas has also migrated updip along carrier beds, but specifically from south

to north, i.e. from the forelimb of the more inward structures to the crest of the more outward ones. The lack of BSRs northward of BSRs 2-to-6 extends this argument from the anticlinal scale to the basin-scale (Fig. 1B) suggesting that deep migration avenues are strictly limited to the southernmost portion of the basin.

5 Conclusion and implications

The SFB hosts a working petroleum system and a number of GH deposits, which are controlled by thermogenic and microbial sources. The specific interplay between structuration, depositional environment and hydrocarbon availability and type, results in the hydrate deposits exhibiting two contrasting distributions which appear to be primarily controlled by the migration mechanism (i.e. advection of free gas vs. in aqueous solution).

In geologic settings where the generation of shallow microbial gas is limited or absent, the distribution of BSR is inferred to be patchy and mostly controlled by deep structures and dipping carrier beds. This, as observed in the SFB, has been inferred also in other geological settings such as the NW Borneo Margin (Paganoni et al., 2018), the Vestnesa Ridge (Smith et al., 2014), and the Barents Sea (Ostanin et al., 2013), with conventional hydrocarbon discoveries occasionally occurring below the relative BSRs. This raises the possibility that in specific geological settings, the source of gas forming gas hydrate deposits can be hinted by the distribution of the BSR by solely using seismic data.

Acknowledgments

We are grateful to Shell International B.V. for sponsoring this project under the Shell-Oxford Research Collaboration. We thank Howard Obee and Bruce Farrer (Borders and Southern Petroleum PLC) for access to seismic and well data and for discussion and review of the manuscript. We thank Schlumberger, CGG and Haliburton for providing free software support. We thank Andy Bell for discussion on the geochemical data. We also thank Barry Katz, Alexei Milkov and an anonymous reviewer for help improving this manuscript significantly.

359

360 **Reference**

- 361 Andresen, K.J., 2012. Fluid flow features in hydrocarbon plumbing systems: What do they tell us about
362 the basin evolution? *Mar. Geol.* 332, 89-108.
- 363 Baba, K., Yamada, Y., 2004. BSRs and associated reflections as an indicator of gas hydrate and free gas
364 accumulation: An example of accretionary prism and forearc basin system along the Nankai
365 Trough, off central Japan. *Resour. Geol.* 54, 11-24.
- 366 Bangs, N.L.B., Sawyer, D.S., Golovchenko, X., 1993. Free gas at the base of the gas hydrate zone in the
367 vicinity of the Chile triple junction. *Geology* 21, 905-908.
- 368 Bear, J., 1972. *Dynamics of Fluids in Porous Media*. Courier Corporation.
- 369 Berg, R.R., 1975. Capillary pressures in stratigraphic traps. *AAPG bulletin*, 59(6), pp.939-956.
- 370 Bergamaschi, B.A., Tsamakis, E., Keil, R.G., Eglinton, T.I., Montluçon, D.B., Hedges, J.I., 1997. The
371 effect of grain size and surface area on organic matter, lignin and carbohydrate concentration, and
372 molecular compositions in Peru Margin sediments. *Geochim. Cosmochim. Acta* 61, 1247-1260.
- 373 Borders and Southern, 2018. Darwin Independent Evaluation, url:
374 [https://ir.euroinvestor.com/Tools/newsArticleHTML.aspx?solutionID=2134&customerKey=bord](https://ir.euroinvestor.com/Tools/newsArticleHTML.aspx?solutionID=2134&customerKey=bordersandsouthern&storyID=13828881&language=en)
375 [ersandsouthern&storyID=13828881&language=en](https://ir.euroinvestor.com/Tools/newsArticleHTML.aspx?solutionID=2134&customerKey=bordersandsouthern&storyID=13828881&language=en)
- 376 Borowski, W.S., 2004. A review of methane and gas hydrates in the dynamic, stratified system of the
377 Blake Ridge region, offshore southeastern North America. *Chem. Geol.* 205, 311-346.
- 378 Boswell, R., Collett, T.S., 2011. Current perspectives on gas hydrate resources. *Energy Env. Sc.* 4, 1206-
379 1215.
- 380 Boswell, R., Frye, M., Shelander, D., Shedd, W., McConnell, D.R., Cook, A., 2012. Architecture of gas-
381 hydrate-bearing sands from Walker Ridge 313, Green canyon 955, and Alaminos canyon 21:
382 northern deepwater Gulf of Mexico. *Mar. Petrol. Geol.* 34, 134-149.
- 383 Boswell, R., Shipp, C., Reichel, T., Shelander, D., Saeki, T., Frye, M., Shedd, W., Collett, T.S.,
384 McConnell, D.R., 2016. Prospecting for marine gas hydrate resources. *Interpretation* 4, SA13-
385 SA24.
- 386 Bry, M., White, N., Singh, S., England, R., Trowell, C., 2004. Anatomy and formation of oblique
387 continental collision: South Falkland basin. *Tectonics* 23.
- 388 Burwicz, E.B., Reichel, T., Wallmann, K., Rottke, W., Haeckel, M., Hensen, C., 2017. 3-D basin-scale
389 reconstruction of natural gas hydrate system of the Green Canyon, Gulf of Mexico. *Geochem.*
390 *Geophys. Geosyst.*
- 391 Cartwright, J.A., Huuse, M., Aplin, A., 2007. Seal bypass systems. *AAPG Bull.* 91, 1141-1166.

392 Cartwright, J. and Santamarina, C., 2015. Seismic characteristics of fluid escape pipes in sedimentary
393 basins: implications for pipe genesis. *Marine and Petroleum Geology*, 65, pp.126-140.

394 Clayton, C., 1992. Source volumetrics of biogenic gas generation. *Bacterial gas*, pp.191-204.

395 Collett, T.S., Johnson, A.H., Knapp, C.C., Boswell, R., 2009. Natural gas hydrates: a review, in: Collett,
396 T.S., Knapp, C.C., Boswell, R. (Eds.), *Natural gas hydrates-Energy Resource Potential and*
397 *Associated Geologic Hazards*, AAPG Memoir, 89, 146-219, pp. 146-219.

398 Crutchley, G.J., Berndt, C., Geiger, S., Klaeschen, D., Papenberg, C., Klaucke, I., Hornbach, M.J., Bangs,
399 N.L., Maier, C., 2013. Drivers of focused fluid flow and methane seepage at south Hydrate Ridge,
400 offshore Oregon, USA. *Geology* 41, 551-554.

401 Crutchley, G.J., Fraser, D.R.A., Pecher, I.A., Gorman, A.R., Maslen, G., Henrys, S.A., 2015. Gas
402 migration into gas hydrate-bearing sediments on the southern Hikurangi margin of New Zealand.
403 *J. Geophys. Res.: Solid Earth* 120, 725-743.

404 Dumke, I., Burwicz, E.B., Berndt, C., Klaeschen, D., Feseker, T., Geissler, W.H., Sarkar, S., 2016. Gas
405 hydrate distribution and hydrocarbon maturation north of the Knipovich Ridge, western Svalbard
406 margin. *J. Geophys. Res.: Solid Earth* 121, 1405–1424.

407 Fish, P. (2005), Frontier South, East Falkland basins reveal important exploration potential, *Oil and Gas*
408 *Journal*, 45(103), 34–40.

409 Foschi, M., Cartwright, J.A., 2016. South Malvinas/Falkland Basin: Hydrocarbon migration and petroleum
410 system. *Mar. Petrol. Geol.* 77, 124-140.

411 Ghiglione, M.C., Quinteros, J., Yagupsky, D., Bonillo-Martínez, P., Hlebszevtich, J., Ramos, V.A.,
412 Vergani, G., Figueroa, D., Quesada, S., 2010. Structure and tectonic history of the foreland basins
413 of southernmost South America. *Journal of South American Earth Sciences* 29, 262-277.

414 Grauls, D., 2001. Gas hydrates: importance and applications in petroleum exploration. *Marine and*
415 *Petroleum Geology* 18, 519-523.

416 Haacke, R.R., Westbrook, G.K. and Hyndman, R.D., 2007. Gas hydrate, fluid flow and free gas: Formation
417 of the bottom-simulating reflector. *Earth and Planetary Science Letters*, 261(3-4), pp.407-420.

418 Haworth, J.H., Sellens, M. and Whittaker, A., 1985. Interpretation of hydrocarbon shows using light (C1-
419 C5) hydrocarbon gases from mud-log data. *AAPG Bulletin*, 69(8), pp.1305-1310.

420 Hedges, J.I., Keil, R.G., Benner, R., 1997. What happens to terrestrial organic matter in the ocean? *Org.*
421 *Geochem.* 27, 195-212.

422 Hillman, J.I.T., Cook, A.E., Sawyer, D.E., Küçük, H.M., Goldberg, D.S., 2017. The character and
423 amplitude of ‘discontinuous’ bottom-simulating reflections in marine seismic data. *Earth Planet.*
424 *Sci. Lett.* 459, 157-169.

425 Hillman, J.I., Burwicz, E., Zander, T., Bialas, J., Klaucke, I., Feldman, H., Drexler, T. and Awwiller, D.,
426 2018. Investigating a gas hydrate system in apparent disequilibrium in the Danube Fan, Black Sea.
427 *Earth and Planetary Science Letters*, 502, pp.1-11.

428 Holbrook, W.S., Hoskins, H., Wood, W.T., Stephen, R.A., Lizarralde, D., 1996. Methane hydrate and free
429 gas on the Blake Ridge from vertical seismic profiling. *Science* 273, 1840.

430 Hovland, M., Gudmestad, O.T., 2001. Potential influence of gas hydrates on seabed installations, in: Paull,
431 C.K., Dillon, W.P. (Eds.), *Natural gas hydrates: occurrence, distribution, and detection*, AGU
432 *Geophysical Monograph* 124, 307-315, pp. 307-315.

433 Judd, A.G., Hovland, M., 2007. *Seabed Fluid Flow: The Impact on Geology, Biology and the Marine*
434 *Environment*. Cambridge University Press.

435 Koenitz, D., White, N., McCave, I.N., Hobbs, R., 2008. Internal structure of a contourite drift generated
436 by the Antarctic Circumpolar Current. *Geochem. Geophys. Geosyst.* 9.

437 Kroeger, K.F., Plaza-Faverola, A., Barnes, P.M., Pecher, I.A., 2015. Thermal evolution of the New
438 Zealand Hikurangi subduction margin: impact on natural gas generation and methane hydrate
439 formation—a model study. *Mar. Petrol. Geol.* 63, 97-114.

440 Liu, X. and Flemings, P.B., 2006. Passing gas through the hydrate stability zone at southern Hydrate Ridge,
441 offshore Oregon. *Earth and Planetary Science Letters*, 241(1-2), pp.211-226.

442 Løseth, H., Gading, M., Wensaas, L., 2009. Hydrocarbon leakage interpreted on seismic data. *Mar. Petrol.*
443 *Geol.* 26, 1304-1319.

444 Magoon, L.B., Dow, W.G., 1994. *The Petroleum System: Chapter 1: Part I. Introduction*.

445 Malinverno, A., 2010. Marine gas hydrates in thin sand layers that soak up microbial methane. *Earth*
446 *Planet. Sci. Lett.* 292, 399-408.

447 Malinverno, A., Goldberg, D.S., 2015. Testing short-range migration of microbial methane as a hydrate
448 formation mechanism: Results from Andaman Sea and Kumano Basin drill sites and global
449 implications. *Earth Planet. Sci. Lett.* 422, 105-114.

450 McConnell, D.R., Zhang, Z., Boswell, R., 2012. Review of progress in evaluating gas hydrate drilling
451 hazards. *Mar. Petrol. Geol.* 34, 209-223.

452 Milkov, A.V., 2005. Molecular and stable isotope compositions of natural gas hydrates: a revised global
453 dataset and basic interpretations in the context of geological settings. *Org. Geochem.* 36, 681-702.

454 Milkov, A.V., Claypool, G.E., Lee, Y.J. and Sassen, R., 2005. Gas hydrate systems at Hydrate Ridge
455 offshore Oregon inferred from molecular and isotopic properties of hydrate-bound and void gases.
456 *Geochimica et Cosmochimica Acta*, 69(4), pp.1007-1026.

457 Milkov, A.V. and Etiope, G., 2018. Revised genetic diagrams for natural gases based on a global dataset
458 of > 20,000 samples. *Organic Geochemistry*, 125, pp.109-120.

459 Nole, M., Daigle, H., Cook, A.E., Hillman, J.I.T., Malinverno, A., 2017. Linking basin-scale and pore-
460 scale gas hydrate distribution patterns in diffusion-dominated marine hydrate systems. *Geochem.*
461 *Geophys. Geosyst.* 18.

462 Ostanin, I., Anka, Z., di Primio, R., Bernal, A., 2013. Hydrocarbon plumbing systems above the Snøhvit
463 gas field: structural control and implications for thermogenic methane leakage in the Hammerfest
464 Basin, SW Barents Sea. *Mar. Petrol. Geol.* 43, 127-146.

465 Paganoni, M., Cartwright, J.A., Foschi, M., Shipp, R.C., Van Rensbergen, P., 2016. Structure II gas
466 hydrates found below the bottom-simulating reflector. *Geophys. Res. Lett.* 43.

467 Paganoni, M., Cartwright, J.A., Foschi, M., Shipp, C.R., Van Rensbergen, P., 2018. Relationship between
468 fluid-escape pipes and hydrate distribution in offshore Sabah (NW Borneo). *Mar. Geol.* 395, 82-
469 103.

470 Pérez, L.F., Hernández-Molina, F.J., Esteban, F.D., Tassone, A., Piola, A.R., Maldonado, A., Preu, B.,
471 Violante, R.A., Lodolo, E., 2015. Erosional and depositional contourite features at the transition
472 between the western Scotia Sea and southern South Atlantic Ocean: links with regional water-mass
473 circulation since the Middle Miocene. *Geo-Mar. Lett.* 35, 271-288.

474 Platt, N.H., Philip, P.R., 1995. Structure of the southern Falkland Islands continental shelf: initial results
475 from new seismic data. *Mar. Petrol. Geol.* 12, 759-771.

476 Plaza-Faverola, A., Bünz, S., Mienert, J., 2012. The free gas zone beneath gas hydrate bearing sediments
477 and its link to fluid flow: 3-D seismic imaging offshore mid-Norway. *Mar. Geol.* 291, 211-226.

478 Pohlman, J.W., Kaneko, M., Heuer, V.B., Coffin, R.B., Whiticar, M., 2009. Methane sources and
479 production in the northern Cascadia margin gas hydrate system. *Earth Planet. Sci. Lett.* 287, 504-
480 512.

481 Posamentier, H.W., Martinsen, O.J., 2011. The character and genesis of submarine mass-transport
482 deposits: Insights from outcrop and 3D seismic data, in: Shipp, R.C., Weimer, P., Posamentier,
483 H.W. (Eds.), *Mass-Transport Deposits in Deepwater Settings*. SEPM Special publication, 96, 7-38,
484 pp. 7-38.

485 Rebesco, M., Hernández-Molina, F.J., Van Rooij, D., Wåhlin, A., 2014. Contourites and associated
486 sediments controlled by deep-water circulation processes: state-of-the-art and future
487 considerations. *Mar. Geol.* 352, 111-154.

488 Riedel, M., Collett, T., Kumar, P., Sathe, A., Cook, A., 2010a. Seismic imaging of a fractured gas hydrate
489 system in the Krishna–Godavari Basin offshore India. *Mar. Petrol. Geol.* 27, 1476-1493.

490 Riedel, M., Collett, T.S., Malone, M.J., 2010b. Expedition 311 synthesis: scientific findings, *Proceedings*
491 *of the Integrated Ocean Drilling Program Expedition*, 311.

492 Riedel, M., Novosel, I., Spence, G.D., Hyndman, R.D., Chapman, R.N., Solem, R.C., Lewis, T., 2006.
493 Geophysical and geochemical signatures associated with gas hydrate–related venting in the
494 northern Cascadia margin. *Geol. Soc. Am. Bull.* 118, 23-38.

495 Ruffine, L., Caprais, J.-C., Bayon, G., Riboulot, V., Donval, J.-P., Etoubleau, J., Birot, D., Pignet, P.,
496 Rongemaille, E., Chazallon, B., 2013. Investigation on the geochemical dynamics of a hydrate-
497 bearing pockmark in the Niger Delta. *Mar. Petrol. Geol.* 43, 297-309.

498 Ruppel, C.D., Kessler, J.D., 2017. The Interaction of Climate Change and Methane Hydrates. *Rev.*
499 *Geophys.* 55, 1-43.

500 Shedd, W., Boswell, R., Frye, M., Godfriaux, P., Kramer, K., 2012. Occurrence and nature of “bottom
501 simulating reflectors” in the northern Gulf of Mexico. *Mar. Petrol. Geol.* 34, 31-40.

502 Schoell, M., 1983. Genetic characterization of natural gases. *AAPG bulletin*, 67(12), pp.2225-2238.

503 Sloan, E. D.; Koh, C. A. 2008. *Clathrate Hydrates of Natural Gases*; CRC Press: Boca Raton.

504 Smith, A.J., Mienert, J., Bünz, S., Greinert, J., 2014. Thermogenic methane injection via bubble transport
505 into the upper Arctic Ocean from the hydrate-charged Vestnesa Ridge, Svalbard. *Geochem.*
506 *Geophys. Geosyst.* 15, 1945-1959.

507 Taladay, K., Boston, B., Moore, G.F., 2017. Gas-In-Place Estimate for Potential Gas Hydrate Concentrated
508 Zone in the Kumano Basin, Nankai Trough Forearc, Japan. *Energies* 10, 1552.

509 Wallmann, K., Aloisi, G., Haeckel, M., Obzhairov, A., Pavlova, G., Tishchenko, P., 2006. Kinetics of
510 organic matter degradation, microbial methane generation, and gas hydrate formation in anoxic
511 marine sediments. *Geochim. Cosmochim. Acta* 70, 3905-3927.

512 Widess, M.B., 1973. How thin is a thin bed? *Geophysics* 38, 1176-1180.

513 Xu, W., Ruppel, C.D., 1999. Predicting the occurrence, distribution, and evolution of methane gas hydrate
514 in porous marine sediments. *J. Geophys. Res.: Solid Earth* 104, 5081-5095.

515

516 **Table 1a**

station	mm	phi	Median	Sorting	Skewness	Kurtosis	fines	sand	gravel
1	0.564	0.83	0.437	2.36	-0.10	1.30	8.8%	71.1%	20.2%
2	0.276	1.86	0.351	2.26	0.29	1.58	15.9%	76.3%	7.8%
3	0.328	1.61	0.282	3.23	-0.01	0.91	20.9%	52.9%	26.3%
4	0.109	3.19	0.116	1.21	0.29	1.63	18.7%	81.1%	0.2%
5	0.068	3.89	0.093	2.52	0.21	1.15	38.6%	57.7%	3.7%
6	0.128	2.97	0.167	2.59	0.16	1.63	24.3%	65.4%	10.3%
7	0.276	1.86	0.130	3.27	-0.31	2.05	23.1%	58.5%	18.3%
8	0.093	3.43	0.120	1.75	0.39	1.55	25.3%	71.5%	3.2%
10	0.169	2.56	0.240	2.03	0.43	1.43	20.0%	76.7%	3.3%
11	0.172	2.54	0.197	2.51	0.08	1.71	21.0%	66.0%	13.1%
12	0.036	4.79	0.048	1.98	0.32	1.01	59.7%	40.3%	0.0%
13	0.031	4.99	0.036	1.93	0.18	0.97	67.3%	32.7%	0.0%
14	0.061	4.03	0.078	3.07	0.08	1.08	46.6%	43.9%	9.5%
15	0.063	3.98	0.091	1.70	0.50	1.45	32.4%	67.6%	0.0%
16	0.101	3.31	0.111	1.31	0.34	1.64	22.1%	77.8%	0.1%
17	0.202	2.31	0.229	1.60	0.27	1.31	13.8%	83.6%	2.6%
18	0.138	2.86	0.150	1.26	0.37	1.77	14.2%	85.8%	0.0%
19	0.335	1.58	0.427	2.31	0.34	1.18	15.6%	79.1%	5.3%
20	0.180	2.48	0.171	2.63	-0.06	1.91	21.0%	63.7%	15.3%
21	0.070	3.83	0.101	2.07	0.35	1.06	35.5%	60.3%	4.2%
22	0.093	3.42	0.116	2.93	0.14	0.86	42.1%	53.1%	4.9%
23	0.024	5.41	0.026	1.88	0.15	1.07	79.0%	21.0%	0.0%

517 Particle size distribution obtained from analysis of surface samples collected at the 23 stations at the
518 seabed (see Fig. 1B for station location).

519 **Table 1b**

station	Moisture Content %	Total Organic Matter %	TOC %	Total Carbonates (%)	Proportion TOC (%)
1	32.6	4.28	0.31	1.73	7.2%
2	31.9	3.38	0.22	3.73	6.5%
3	27.2	3.69	0.32	2.49	8.7%
4	27.6	2.57	0.26	1.50	10.1%
5	34.1	3.45	0.18	2.70	5.2%
6	31.2	3.97	0.33	2.37	8.3%
7	33.3	2.71	0.27	1.97	10.0%
8	35.6	3.08	0.22	1.76	7.1%
10	28.7	4.24	0.40	2.29	9.4%
11	27.8	3.95	0.23	2.14	5.8%
12	39.7	3.09	0.46	1.97	14.9%
13	45.1	3.55	0.51	2.12	14.4%
14	31.0	4.43	0.35	1.56	7.9%
15	31.4	3.00	0.36	1.70	12.0%
16	27.8	2.52	0.29	1.48	11.5%
17	27.4	2.64	0.21	1.39	8.0%
18	30.2	2.83	0.24	1.51	8.5%
19	26.3	3.76	0.31	3.60	8.2%
20	26.1	3.63	0.23	2.46	6.3%
21	34.5	3.75	0.31	1.73	8.3%
22	33.3	4.58	0.32	1.37	7.0%
23	33.0	3.90	0.60	1.99	15.4%

520

521 Summary of moisture content, inorganic and organic carbon components of samples collected at the 23
522 stations at the seabed (see Fig. 1B for station location).

Fig. 1. Location map of the Falkland Islands (FI), Falkland Plateau Basin (FPB), South Falkland Basin (SFB) and Scotia - South American Plate Boundary (SSAPB), with positions of the study area (B) and contour of the bathymetry (A). Bathymetry of the study area with position of seabed landslides (SL), positions of the bottom simulating reflections (BSRs), location of wells 61/17-1 and 61/25-1, benthic stations (white dots) and 2D seismic lines shown in this study (B). Interpreted seismic section depicting the main structural and stratigraphic elements of the Interval of Interests, including mass transport deposits (MTD), seabed depressions (SD) and mini-basins (MB). Interpreted bottom simulating reflectors (BSR, black-white-black, b-w-b; inset) and location of the benthic stations and well 61/25-1 (p. = projected) (C). Distribution of the BSR in the foreland and in the thrust-fold anticlines based on Foschi and Cartwright (2016) and this study (D).

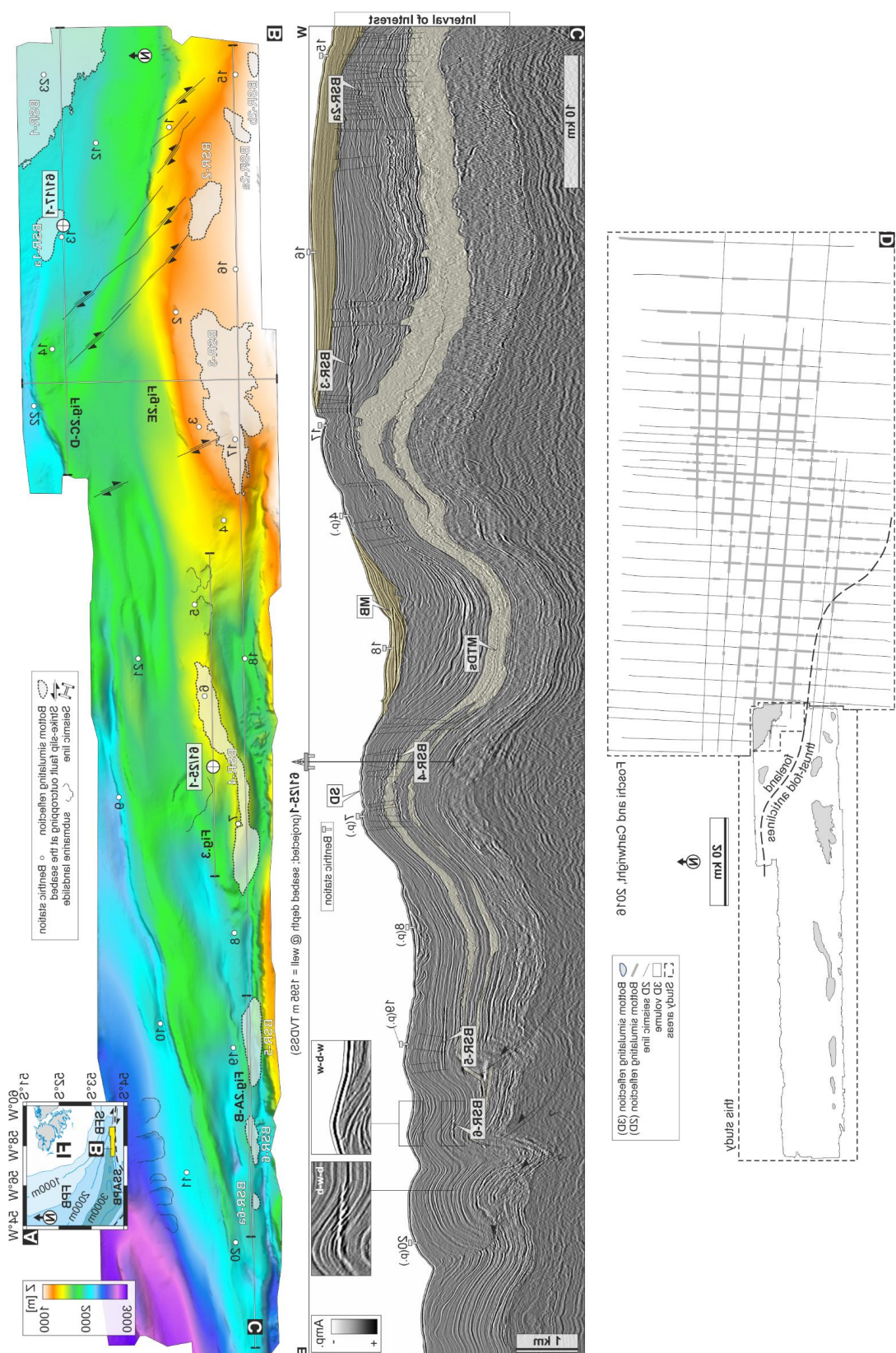
Fig. 2. 2D seismic cross-sections showing the bottom simulating reflectors (BSRs) in the study area (refer to Fig. 1B for line location). BSRs 5, 6 and 6a occur within the core of three anticlines and at about 300-400 m below the seabed. The BSRs occur along the modelled base of the gas hydrate stability zone (mBGHSZ) consistent with 100% methane and geothermal gradient of $55^{\circ}\text{C} \cdot \text{km}^{-1}$ (BSR-5) and $40\text{--}50^{\circ}\text{C} \cdot \text{km}^{-1}$ (BSRs 6, 6a). Below the free gas zone 6 (FGZ-6) bright dipping soft anomalies are interpreted as gas charged layers. These are bright in amplitude up to the base of the FGZ where an abrupt change of amplitude can be observed (A). BSRs 5, 6 and 6a appear flat on the seabed-flattened 3D seismic cube. In this cross section a discordant pattern can be observed on BSR-6 although the depth of the seabed changes just slightly. The vertical distance between the BSRs and the seabed changes from west to east. This is interpreted to be related to erosion at the seabed, highlighted by the interpreted red horizon which divides a portion of the overburden and which is completely eroded in the western portion of this cross section. This specific section (station 19) exhibits low total organic carbon (TOC) in the sediments near the seabed (B). BSR-1 occurs within mass transport deposits (MTDs) within the young sedimentary infill of the foreland basin. FGZ-1 is interpreted from the increase of acoustic response located just beneath the BSR. The base of FGZ-1 is not present. The benthic stations from west to east show a systematic decrease of TOC from the foreland to the crest of anticline to the east (C). Close up from Fig. 2C. At the well 61/17-1 a geothermal gradient of $35.47^{\circ}\text{C} \cdot \text{km}^{-1}$ was measured. BSR-1 falls along the mBGHSZ with similar geothermal gradient and with a gas composition of 100% (D). BSR-3 is hosted by southward dipping contourite sheets. A region of acoustic amplification interpreted as FGZ. BSR-3 fall along the mBGHSZ consistent with a geothermal gradient of $45^{\circ}\text{C} \cdot \text{km}^{-1}$. TOC above BSR-3 and along the anticlines is lower with respect to stations in the foreland basin (E).

Fig. 3. Composite figure depicting the main acoustic feature of BSR-4, total organic carbon (TOC) profile and gas wetness at well 61/25-1. The BSR-4 (refer to Fig. 1B for location) is located within the core of the anticline at about 300 m below the seabed. A number of amplitude anomalies (AAs) are observed below BSR-4 and potentially related to free gas. BSR-4 falls along the modelled base of the gas hydrate stability zone at $50^{\circ}\text{C} \cdot \text{km}^{-1}$ although just 1.8 km distance from the BSR-4 the borehole 61/25-1 recorded a geothermal gradient of $\sim 29^{\circ}\text{C} \cdot \text{km}^{-1}$. TOC at the seabed ranges from 0.18 to 0.33% (A). TOC profile integrated with stations at the seabed shows a linear increase of organic carbon with depth. Measurements are interrupted at the mass transport deposit (MTD) (B). Gas wetness (Wh, c.f. Haworth et al., 1985) measured on gas samples from IsoJar and IsoTube methods (see text). The wetness of the gas increase towards the inner portion of the anticline. $\delta^{13}\text{C}$ data were retrieved from methane collected from IsoJars (C; see also Fig. 4A).

Fig. 4. Genetic diagram of $\delta^{13}\text{C}\text{-C}_1$ versus $\text{C}_1/(\text{C}_2 + \text{C}_3)$ (after Milkov and Etiope, 2018) (A) for gas samples collected by IsoJars at well 61/25-01 (B). The gas composition varies from early mature thermogenic (EMT) towards late mature thermogenic (LMT) from the shallow to the inner portion of the anticline (with depth). The increase in $\text{C}_1/(\text{C}_2 + \text{C}_3)$ of samples #4-#7 with depth may indicate the presence of secondary microbial gas from biodegradation of petroleum towards the inner portion of the anticlines. EMT = early mature thermogenic gas; F = methyl-type fermentation; OA = oil-associated thermogenic gas; SM = secondary microbial.

Fig. 5. Simplified cartoons showing the evolution of the foreland region of the South Falkland Basin (indicative), the distribution and generation of microbial gas (A and B), and the formation of a laterally continuous BSR. A higher percentage of total organic carbon (TOC) is expected to be present in this region, as observed by its generally higher content at the seabed. Microbial gas in excess of saturation (free gas) is, therefore, more likely to occur (see text). Microbial gas formed initially in solution in the pore water will be further diffuse until a condition of super saturation occurs. Segregation of free gas within the gas hydrate stability zone will form gas hydrates.

Fig. 6. Simplified cartoons showing the evolution of the thrust and fold anticlinal region of the South Falkland Basin (indicative) and migration of thermogenic gas and the formation of a restricted BSR. Microbial gas is probably not sufficient to produce gas in excess of saturation (A), therefore thermogenic gas and secondary microbial gas present in this part of the basin migrate towards the seabed generating the observed gas hydrate stability zones and the free gas zone (B). The pathways for gas migration are likely to be southward dipping carrier beds. Cross stratal migration may also concur to the delivery of gas towards the seabed. Importantly these migration pathway will restrict the production of gas hydrates only on those areas where the migrating gas intersect the base of the gas hydrate stability zone.



590 Figure 2

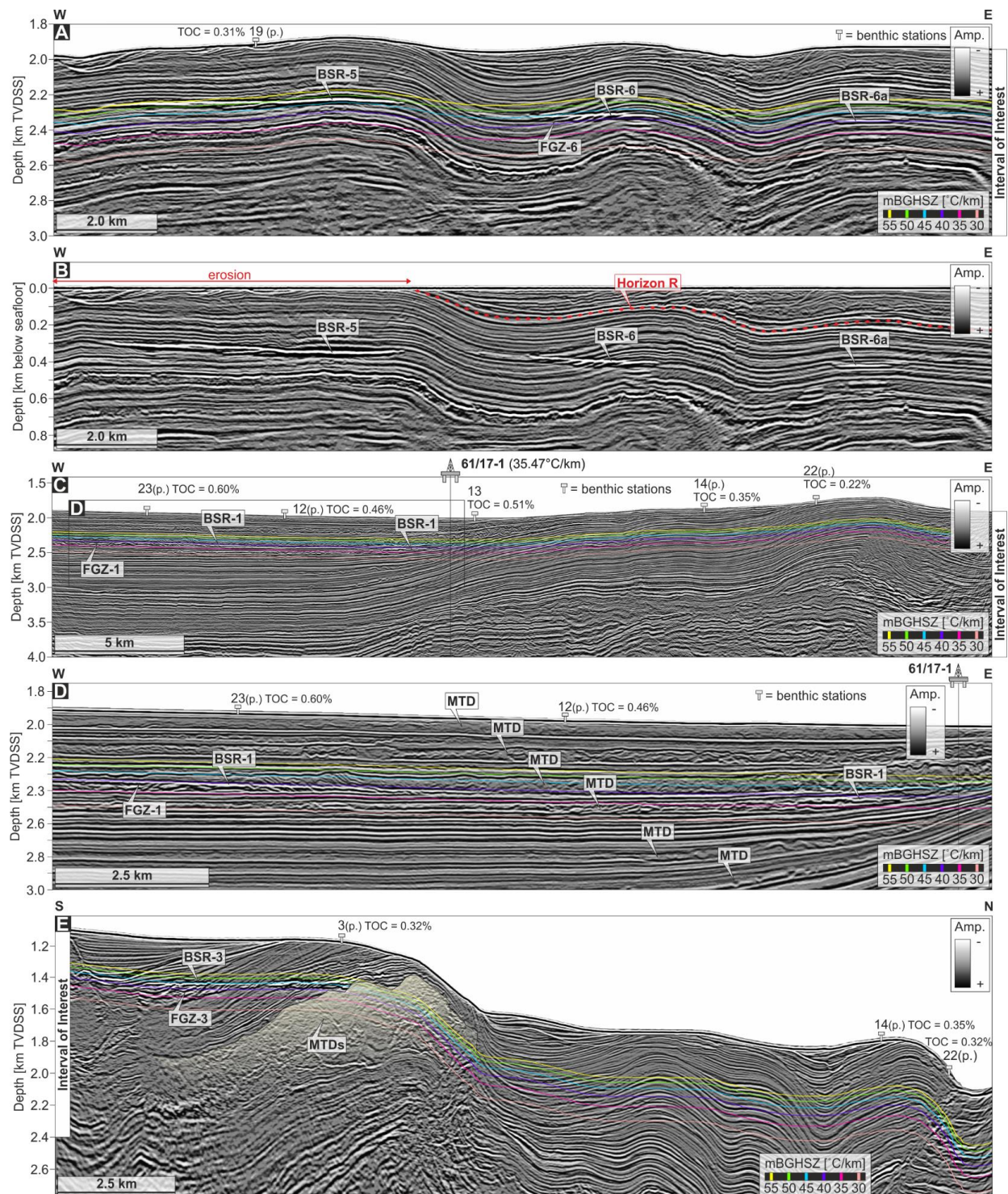
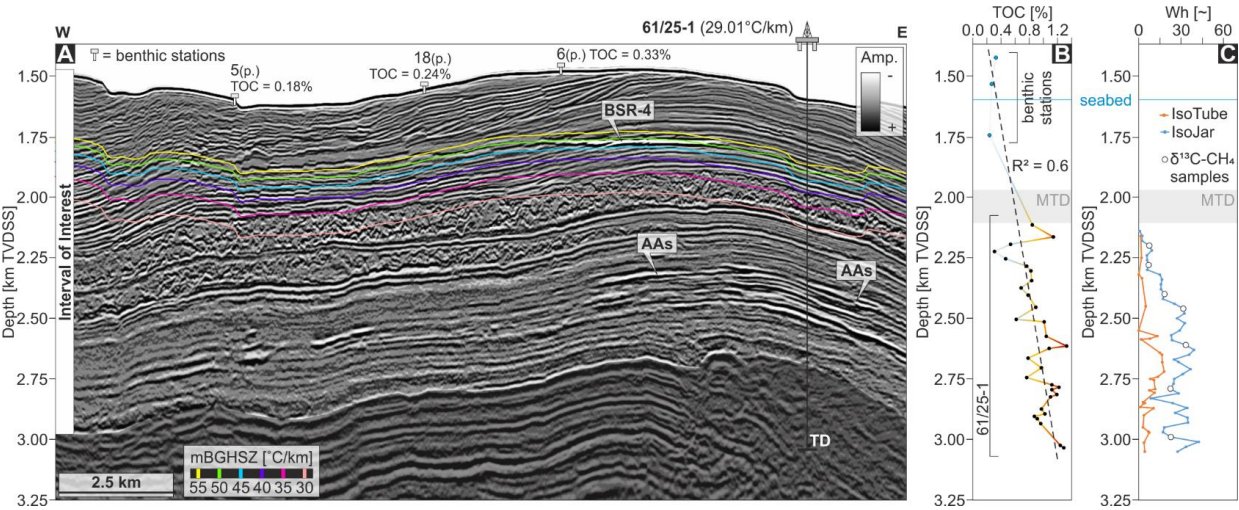
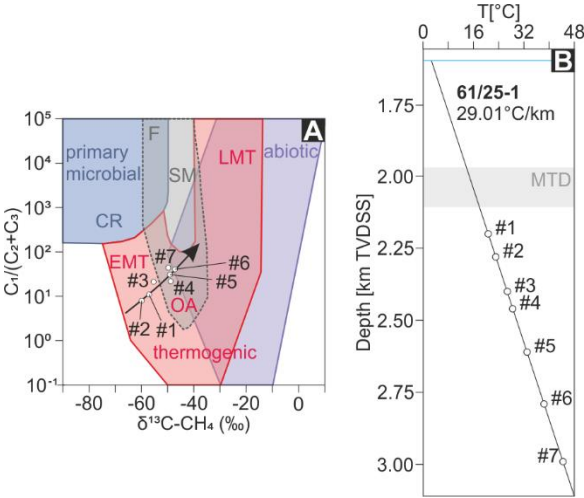


Figure 3



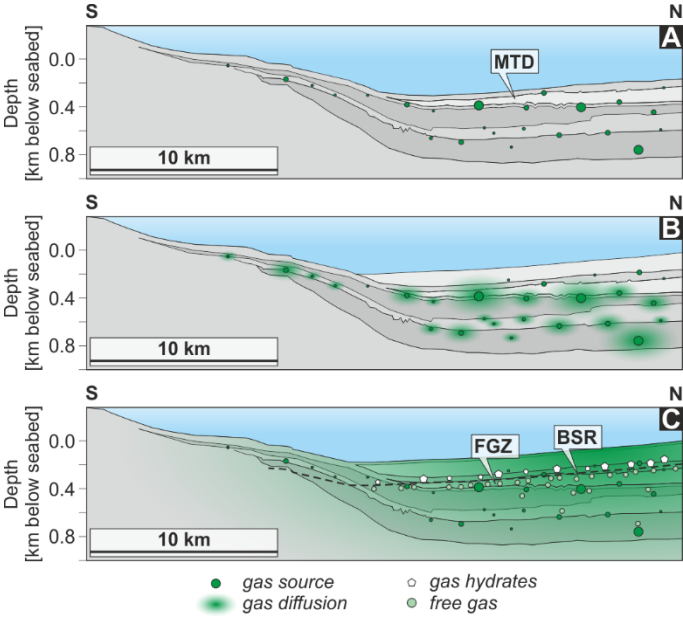
596 Figure 4



597

598

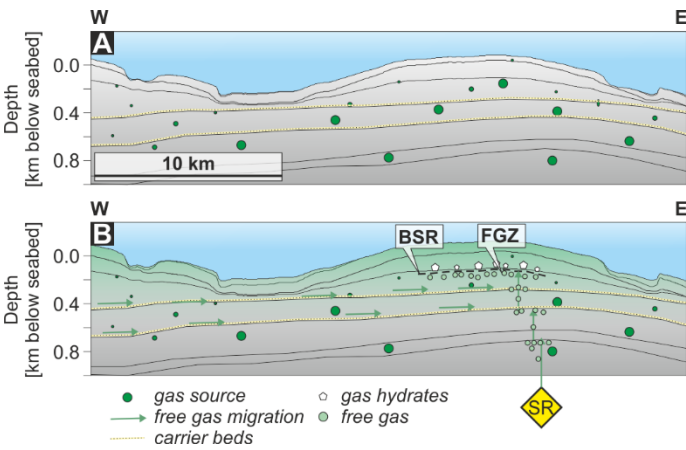
599 Figure 5



600

601

602 Figure 6



603